
Numerical Investigation of Characterization of Thick Cryogenic-Fuel Layers Using Convergent Beam Interferometry

The effect of hydrodynamic instabilities on the performance of inertial confinement fusion (ICF) experiments is well known. Hydrodynamic instabilities affect ICF capsules during the initial acceleration and final deceleration phases of the implosion. Nonuniformities in the applied drive coupled with imperfections at the target surface seed Rayleigh–Taylor (RT) unstable growth at the ablation front. In addition, the shock wave reflecting off a perturbed inner ice surface returns to the ablation region and also seeds the instability (feed-out). These perturbations grow since low-density, ablated material accelerates the unablated, dense shell. Further growth of these perturbations eventually feeds through the shell and couples with existing perturbations on the inner ice surface. Together these seed RT growth at the ice–gas interface when the ice layer begins to decelerate around the spark plug region near the target’s center. As the RT instabilities grow, the cold, dense fuel is mixed into the hot core leading to cooling of the core and reduced target performance.

The success of the ICF program depends on targets designed to limit the amount of RT growth to an acceptable value or whose performance is insensitive to the presence of such perturbations. A good understanding of all nonuniformity sources in the implosion is required to design such targets. Nonuniformity sources include the laser or holhraum drive, the coupling of this energy to the target (imprint), and the initial surface finish of both the outer ablator surface and the inner DT ice. To date, significant progress has been made in understanding the role of the first three nonuniformity sources. Characterization of the inner ice surface, however, remains a serious challenge. The ability to accurately characterize this surface is especially critical in light of recent work by Betti¹ in which the feed-out contribution to the ablation region has been shown to be a major factor in overall RT growth during an implosion.

Overview

Cryogenic targets imploded with OMEGA will consist of polymer capsules several micrometers thick with diameters ranging from 900 to 1100 μm . These capsules will be filled with condensed D_2 or DT fuel up to 100 μm thick. Historically,

the fuel content and fuel-layer uniformity of cryogenic targets at LLE have been interferometrically characterized using plane-wave illumination.^{2–7} A capsule with a thick cryogenic layer condensed on its interior behaves as a strong negative lens, which has several adverse effects on an interferogram created with plane-wave illumination. Computer simulations of typical interferograms are shown in Fig. 79.14. The highly divergent and spherically aberrated wavefront created by the target cannot be effectively collected and imaged by optics with convenient numerical apertures (<0.2), resulting in loss of information near the perimeter of the target’s image. Additionally, interfering this highly curved wavefront with a planar reference wavefront results in an interferogram with a fringe spatial frequency that increases radially to very high values near the perimeter of the target’s image. The phase sensitivity

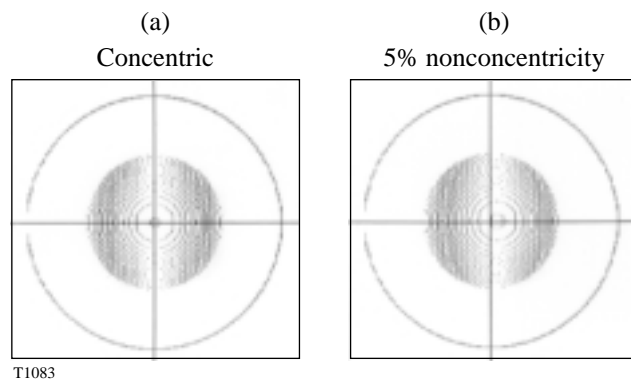
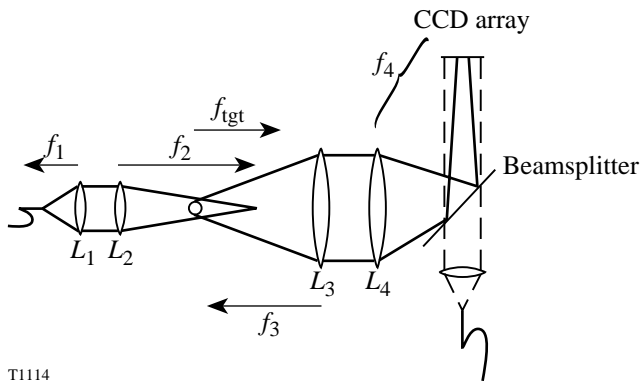


Figure 79.14
Computer-generated interferograms of a 1120- μm -diam, 10- μm -thick capsule that contains 100 μm of condensed fuel. These interferograms were created assuming that both the object and reference beams consisted of planar wavefronts with a 514-nm wavelength, and that $f/6$ optics were used to image the target. All of the surfaces in (a) were perfectly concentric with one another, whereas (b) displays a 5% fuel nonconcentricity, i.e., the center of the spherical inner surface of the condensed fuel layer has been displaced to the right in the figure by 5% of its total thickness. Obviously, a 5% nonconcentricity can be easily detected, but higher-order nonuniformities are much more difficult to detect due to the very high fringe frequency. In addition, information regarding the state of the fuel near the perimeter of the target’s image has been lost due to refraction of the object beam outside of the imaging optics’ finite collection aperture.

is reduced dramatically when the fringe frequency approaches the Nyquist limit of the detector. As the fringe frequency nears the frequency of pixels in the CCD array, aliasing occurs and the fringes become unresolved.

These limitations can be compensated for by focusing the object beam of a Mach-Zehnder interferometer near the rear focal point of the filled target, causing a nearly collimated beam to emerge. A complete description of this interferometer has been published elsewhere.⁸ The optical system used to create an interferogram of a cryogenic target with convergent-beam illumination is shown in Fig. 79.15.



T1114

Figure 79.15

Schematic of the optical system used to create an interferogram of a cryogenic target with convergent-beam illumination. The optics that control the point of focus of the convergent beam and those that image the target are shown. The dashed line denotes the collimated reference beam.

Phase sensitivities of the order of a few hundredths of a wave can be achieved by phase-shifting techniques.⁹⁻¹¹ This involves sequentially acquiring multiple interferograms, each with a unique phase offset caused by introducing a slight path-length change in one of the interferometer's arms. The phase of each point in the interferogram is then obtained, modulo 2π , by performing simple mathematical operations on the set of interferograms. One advantage of phase-shifting methods is that the phase resolution depends primarily on the dynamic range of the CCD array and the contrast of the interferogram, not the number of pixels per fringe.

Methodology

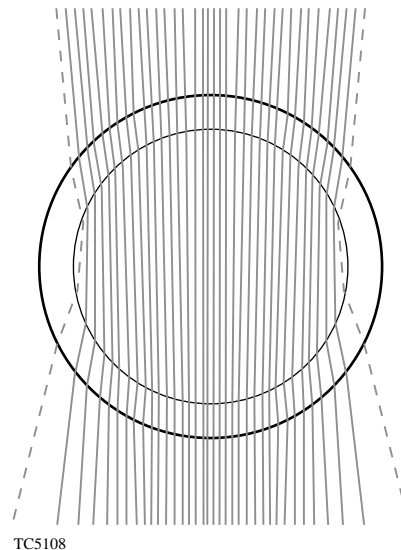
Characterizing a nonuniform cryogenic-fuel layer by interpreting the phase of a wavefront perturbed by passing through it is, unfortunately, not straightforward. Evident in Fig. 79.16, the majority of rays traveling through the target have probed two independent ice surfaces on opposite sides of the target.

Unique measurement of a perturbation on either surface is impossible without collecting an enormous number of interferograms.

The method we propose is very similar to the technique implemented by Wallace¹² to characterize surface perturbations on the outside of ICF capsules. Data is first collected using atomic force microscopy (AFM) along great circles on the target surface. This information is Fourier-analyzed to produce an average one-dimensional (1-D) power spectrum. The 1-D Fourier power spectrum is then mapped into the two-dimensional (2-D) spherical-harmonic spectrum by using an Abel transformation derived by Pollaine.¹³ Pollaine showed that a 1-D Fourier power spectrum, representative of the entire surface, could be transformed into the corresponding 2-D power spectrum using

$$P_{2-D}(l) = \frac{d}{dl} \int P_{1-D}(\sqrt{l^2 + n^2}) dn.$$

MacEachern¹⁴ showed that a representative 1-D power spectrum could be obtained by averaging nine independent, experimental 1-D power spectra together. These nine traces are



TC5108

Figure 79.16

Ray trace of an $f/5$ laser through an OMEGA cryogenic capsule. The method uses rays very near the perimeter of the target similar to the dashed rays in the figure. Such rays probe two points on the inner surface, which, when averaged, represent two of the scans used in the outer-surface-measurement technique described in the text.

arranged in groups of three and are taken along great circles that lie on the three orthogonal planes that intersect the target's center. Each set of three traces samples an approximately 40- μm -wide swath on the target's surface. The geometry used in this data-acquisition method is shown in Fig. 79.17 with the three traces within a set labeled A, B, and C.

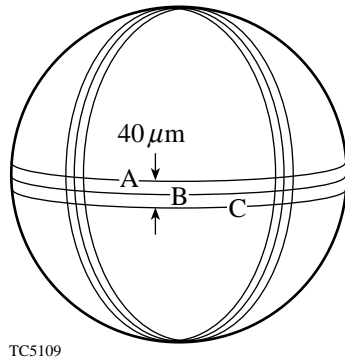


Figure 79.17
 Geometry of data-acquisition traces used in the surface-characterization method. Each of the three sets of traces lies along an orthogonal direction on the sphere. The width between outer traces is approximately 40 μm .

Reexamining Fig. 79.16, it can be seen that there is a subset of rays, traveling very near the equator of the target, where a small cord ($\sim 40 \mu\text{m}$ long) probes two points of the inner ice surface. Such a ray is shown dashed in Fig. 79.16. The perturbed optical-path difference (OPD) along this path represents an average at the two positions. Collecting all of these rays from the overall phase map yields a great circle of data, coming out of the paper, sampling the inner ice surface near the equator at this orientation. This is essentially the same as averaging traces A and C in the method described above and shown in Fig. 79.17. The target is rotated and data is collected along several great circles. This data is analyzed using the process described above for characterizing an outer-surface perturbation spectrum.

Implementation

To implement the characterization method described above, the phase of the wavefront passing through the cryogenic target must be acquired by interferometrically measuring the OPD between it and a planar reference wavefront. Eventually, when the cryogenic filling station at LLE is in operation, this information will be provided by measuring real ICF capsules. Initial analysis, however, has been done using synthetic OPD maps produced using the ray-trace simulation code *Rings*. *Rings*,

which was written by Craxton¹⁵ to simulate three-dimensional (3-D) planar interferometric probes, was modified to provide for a convergent $f/5$ probe at 670 nm. The capsule used in our analysis is equivalent to that of a cryogenic target designed to be used in initial experiments on OMEGA. The capsule consists of a thick shell of DT ice (100 μm) surrounded by a single, thin layer of plastic (1 to 5 μm). Fully independent perturbations can be applied to any or all interfaces within the target. Originally, these perturbations were limited to simple geometric terms of the order of less than 4. Routines have since been added that allow perturbations to be imposed based on their complete spherical-harmonic spectrum. Normalization routines control the total applied ice-surface roughness (rms) and spectral dependency of the modal pattern. Multiple, independent great circles can be simulated by aligning the probe axis with respect to selected points on the target.

Rings determines the intersection of a ray at every physical interface within the target to within 1 \AA . Once the intersections are determined, the total optical path is calculated for the transit through the preceding layer. Snell's Law is then applied to produce the proper change in direction cosines for transit into the next layer. *Rings* traces many rays through the target and into a collection optic. The resulting phase map is then projected back to an image plane located at the center of the target, which is conjugate to the detector plane in the actual interferometer.

The OPD map must first be analyzed to identify a radius that corresponds to the inner ice surface. As can be seen in Fig. 79.16, this information is near the very edge of the map. Rays that intersect the target at steeper angles are refracted outside of the collection aperture of the interferometer's $f/5$ imaging system. Once identified, this information is not necessarily uniformly spaced along a circle; it must then be interpolated to a great circle of 2^n evenly spaced points to be analyzed by standard FFT routines. Many interpolation schemes were tested. A solution was found that imports the data into the commercially available graphics package Tecplot.¹⁶ Tecplot runs on Pentium PC's and has extensive capabilities to interpolate data to a variety of physical grids, including evenly spaced circles. The interpolated data is then Fourier-analyzed to recover a 1-D power spectrum. The overall procedure to analyze a given OPD takes only a few minutes per view. It is anticipated that an averaged 1-D power spectrum, evaluating six views (as shown in Fig. 79.18), could be obtained in less than one-half hour. The final step—transforming the averaged 1-D power spectrum into the 2-D spectrum—is accomplished using a Fortran program and requires only a few minutes of computer time.

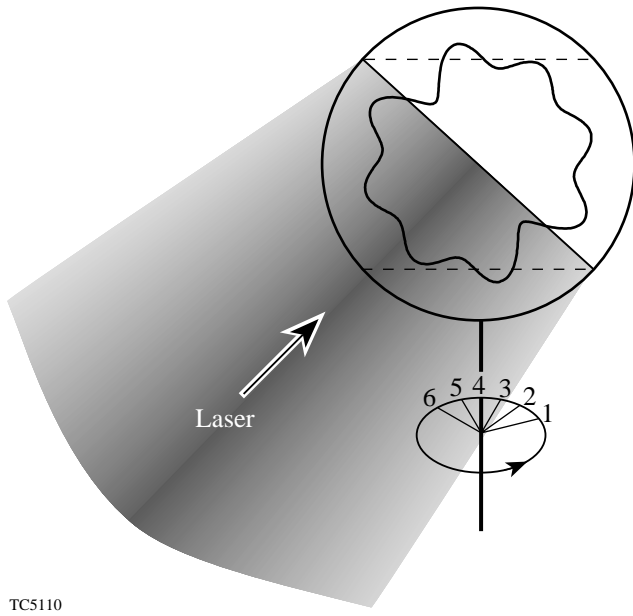


Figure 79.18 Schematic indicating the data-acquisition procedure. The probe laser is incident on the target at an angle of 17.72° below the equator. After collecting data for the position, the target is rotated on-axis 30° and scanned again. The procedure is repeated until six scans are completed.

Numerical Results

The first test of the method described above was to perturb the inner ice layer with pure sinusoidal modes to determine whether the FFT of the great circle of the synthetic OPD would return the applied value. Such a test does not require the Abel transformation. Initially, only single sinusoidal modes ($m = 20, 40, \text{ and } 80$) were modeled. The results, shown in Fig. 79.19, demonstrate that the method is able to reproduce the applied perturbation quite well. The next step was to perturb the target with a whole spectrum of sinusoidal modes given by

$$R_1 = R_0 + \sum a_0 m^{-1.1} \cos\{m[\varphi + 2\pi b(m)]\},$$

where $a_0 = 0.739 \mu\text{m}$ and $b(m)$ is a random number used to distribute random phase among the modes. The result of these tests, shown in Fig. 79.20, indicate that the method is able to recover the applied sinusoidal spectrum very well.

Building on these results, tests were constructed that would more closely match what one would expect in nature. The pertinent values that are required for numerical simulation of ICF capsules are the total rms and the modal dependency of the overall spherical-harmonic spectrum. As such, several ex-

amples were constructed using a variety of total roughness and spectral dependency. The applied perturbations took the form

$$R_1 = R_0 + \sum_{\ell=2}^n \left(\frac{a_0 \ell^{-\beta}}{\sqrt{2\ell+1}} \sum_{m=-\ell}^{\ell} Y_{\ell,m} \right),$$

where n is the number of applied modes, β is the modal dependence of the applied spectrum, and a_0 has been normal-

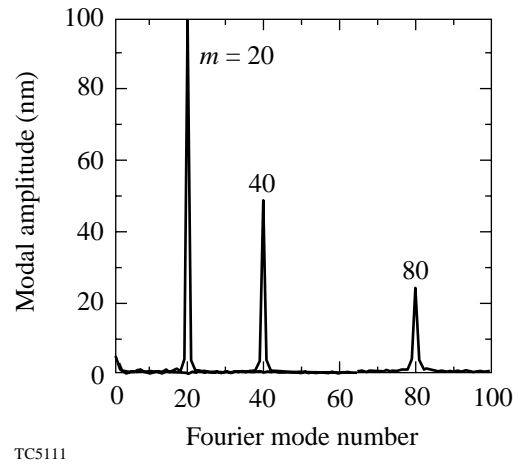


Figure 79.19 Mode amplitudes of OPD determined through ray trace of targets with inner-ice surface perturbed with an individual sinusoidal mode. The amplitudes of the applied perturbations were chosen to scale as $2000/m \text{ nm}$.

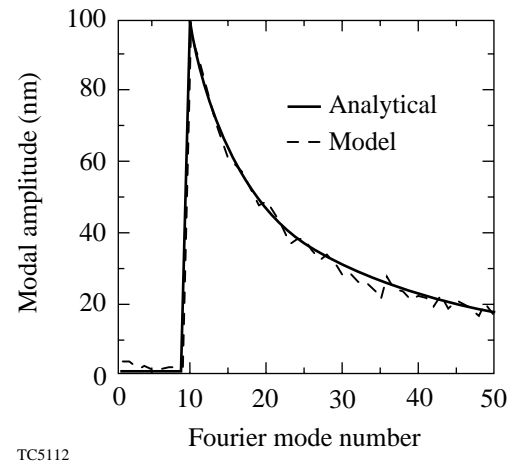


Figure 79.20 Mode amplitudes of OPD determined through ray trace of targets with inner-ice surface perturbed with a spectrum of sinusoidal modes between mode $m = 10$ and $m = 50$. The solid curve represents the exact modal spectrum that was applied to the surface.

ized to return the desired surface rms. The spectral amplitudes were modified in the high-frequency range by applying a Blackman filter¹⁷ to avoid Gibb's phenomenon behavior in the numerical reconstruction of the applied spectrum.

An important point to these calculations is the determination of a cutoff frequency above which any additional modes make little contribution to the overall perturbation at stagnation and, as such, need not be resolved. This cutoff is generally taken to be near mode 50. This cutoff comes from stability arguments of target designs that assume monotonically decreasing perturbation spectra of the order of $\ell^{-\beta}$ at the beginning of the deceleration phase of the implosion. For $\beta = 1.5$, the relative mode amplitudes at about mode 40 and beyond are one to several orders of magnitude lower than the amplitudes of mode numbers below 10. When Haan saturation effects¹⁸ are considered, however, it can be shown that such a cutoff is applicable for perturbation spectra that are even flat ($\beta = 0$) at the onset of deceleration (see Appendix A). Therefore, our analysis, while examining targets with perturbations using modes 2 to 192, resolves only the modal region of the ice roughness between modes 2 and 50.

Similar to the above sinusoidal perturbation tests, our first test with spherical harmonics was to perform an analytical

check of the method. Knowing the analytic form of the perturbation spectrum placed on the inner ice layer, we could immediately take the Fourier transform of the resulting perturbed radius representing the inner target equator. This 1-D power spectrum was then transformed to give back the applied 2-D spectrum. The results of this case are shown in Fig. 79.21, where it can be seen that the method gives very good reconstruction of the applied spectrum except in the very high frequency range. Here the method experiences slight trouble in reconstructing the spectrum. The numerical results here are being strongly influenced by the unphysical termination of the spectrum. The results of this test confirmed that a good approximation of the 2-D spectrum of the inner ice surface could be obtained from ray-trace data that correctly maps a great circle of the inner ice surface.

We then examined ray-trace tests that spanned both the rms of the surface and the modal dependency of the spectrum. The results of one of these tests are reported here. When the spherical harmonics are applied, the amplitude of all m -components of a particular ℓ -mode is assumed constant. Additionally, a base-line total rms value used here is defined to include only the power in modes 10 to 50. Several examples, comparing the numerically obtained modal amplitude spectrum with the exact applied perturbation, are shown in Fig. 79.22. The

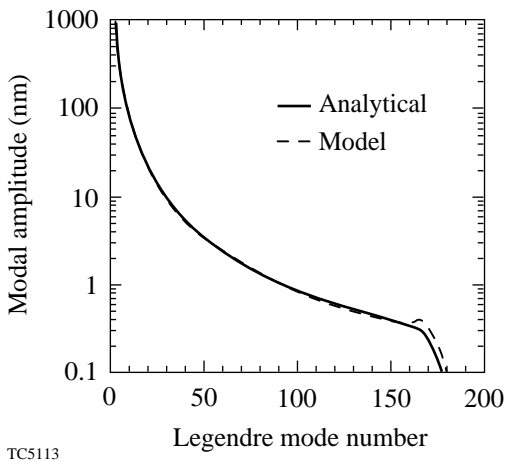


Figure 79.21 Evaluation of an analytical representation of a spherically perturbed inner ice surface. The solid curve represents the exact modal spectrum applied to the surface. The dashed curve is obtained by taking the FFT of the perturbed radius and transforming the 1-D power spectrum into the 2-D power spectrum. Except for the high-frequency regime, the method can be very accurate in resolving the 2-D applied perturbation using 1-D data.

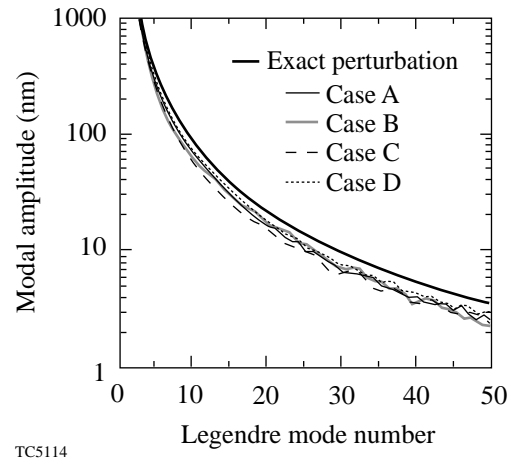


Figure 79.22 Comparison of several ray-trace evaluations of an OMEGA cryogenic capsule with a spherically perturbed inner ice surface. The thick solid curve represents the exact modal spectrum applied to the inner surface. The other curves are obtained by averaging a set (six numerical ray traces) of 1-D power spectra of perturbed OPD and then transforming that average into the 2-D power spectrum. Each curve represents the resulting modal amplitudes obtained at a separate orientation on the target. These orientations are given in Table 79.II.

capsule was perturbed with a full spectrum of modes from $\ell = 2$ to $\ell = 192$. The baseline total rms was set to be $0.25 \mu\text{m}$ with a spectral parameter $\beta = -1.5$. Four tests (Cases A–D) were performed, representing the acquisition of data at different spherical orientations on the capsule. Each case used six acquired ray traces taken about the capsule to produce the average 1-D power spectrum for the analysis. The spherical orientations are given in Table 79.II. Examining Fig. 79.22, it can be seen that each of the tests provides a very good representation of the modal dependency of the applied perturbation. Case B recovered 89% of the total rms defined from modes 2 to 50, while Case C recovered only 73%. From these results, it can be seen that the method provides good resolution of the perturbations on the inner ice surface.

Future Work

The method we have described will provide a detailed analysis of the inner-ice-surface roughness; however, more work must be performed to determine the sensitivity of the method under a variety of physical constraints. Aberrations in the wavefront caused by the optical system have not been included in the model so far. These can potentially be subtracted from the target's phase map by taking a phase map of the wavefront passing through the interferometer without a target present. The shot noise and finite resolution of the CCD array detector (i.e., their role in limiting the phase sensitivity of the interpolation routine) should also be examined. Finally, the limitation that perturbations on the surfaces of the capsule impose on the sensitivity of ice-surface measurements should be examined.

ACKNOWLEDGMENT

This work was supported by the U.S. Department of Energy Office of Inertial Confinement Fusion under Cooperative Agreement No. DE-FC03-92SF19460, the University of Rochester, and the New York State Energy Research and Development Authority. The support of DOE does not constitute an endorsement by DOE of the views expressed in this article.

Appendix A

To determine the critical modes that make up the perturbed interface between the cold, dense fuel and the hot spark-plug region, the RT growth that all modes experience during the deceleration phase in an ICF implosion must be examined. We start by assuming a modal dependency between the modes that is of the form

$$\sigma_\ell = \frac{C_1}{\ell^\beta}.$$

Given the total surface perturbation σ_{rms} , one can integrate over the modes (from 2 to 500) to arrive at the constant C_1 as

$$C_1 = \frac{\sigma_{\text{rms}}}{\sqrt{\sum \frac{1}{\ell^{2\beta}}}}.$$

Lindl¹⁹ has shown that during deceleration any unsaturated modes will grow roughly as

$$a_\ell^{\text{lin}} = (a_\ell)_0 e^\eta,$$

where

$$\eta = \sqrt{\frac{2\ell}{1+0.2\ell}}.$$

One can see that η asymptotes quickly to the value $\eta \cong \sqrt{10} (\sim 3)$ at about mode 20. As such, in the absence of saturation, all modes above 20 will grow roughly the same. If one assumes the initial perturbation spectrum to be comparable to the initial ice surface, the spectral parameter β can be set to be ~ 1.5 . While most of the modes will grow the same, the final amplitudes of modes greater than 40, as shown in Fig. 79.A1, are relatively

Table 79.II: Orientation angles used in numerical ray-trace tests. Cases A and B represent scans at two orthogonal positions on the sphere. Case C was chosen as a neutral position between A and B. Finally, Case D is for scans along the optical axis proposed for the experimental characterization station at LLE.

Case	Orientation Angles (θ, Φ)					
	Scan 1	Scan 2	Scan 3	Scan 4	Scan 5	Scan 6
A	90, 0	90, 30	90, 60	90, 90	90, 120	90, 150
B	90, 90	60, 90	30, 90	0, 90	30, 180	90, 150
C	90, 0	75, 30	60, 60	45, 90	60, 120	75, 150
D	72.28, 0	72.28, 30	72.28, 60	72.28, 90	72.28, 120	72.28, 150

very small. As such, these modes lend no significant contribution to the overall perturbation at stagnation; however, the initial spectrum involved must also include contributions from perturbations feeding through from the ablation surface. These perturbations will add in quadrature with the ice layer, and the resulting perturbation rms will probably no longer obey $\beta = 1.5$. As shown in Fig. 79.A1, the final amplitude spectrum of these perturbations increases monotonically with decreasing β . While it is hard to conceive of β ever being negative, having β approach zero must be considered.

Of course, as the spectral parameter does approach zero, more power is shifted out of the low-order modes and into the higher-frequency modes. These modes will then become can-

didates for saturation. Haan has shown¹⁸ that, for a specific mode, as the amplitude approaches its saturation amplitude

$$\left(a_\ell^{\text{sat}} = \frac{2R}{\ell^2} \right),$$

its RT growth undergoes a transition and stops growing exponentially. The amplitude of this perturbation then grows linearly in time and is given by

$$a_\ell = a_\ell^{\text{sat}} \left[1 + \ln \left(\frac{a_\ell^{\text{lin}}}{a_\ell^{\text{sat}}} \right) \right].$$

Therefore, such modes will grow much slower than unsaturated ones and will not contribute significantly to the overall perturbation at stagnation.

A threshold for saturation can be calculated by comparing the Haan saturation amplitude at a given radius to the given perturbation rms at that point:

$$\frac{2R}{\ell_c^2} = \sqrt{\frac{4\pi}{(2\ell_c + 1)}} \sigma_\ell = C_1 \sqrt{\frac{4\pi}{(2\ell_c + 1)}} \ell_c^{-\beta},$$

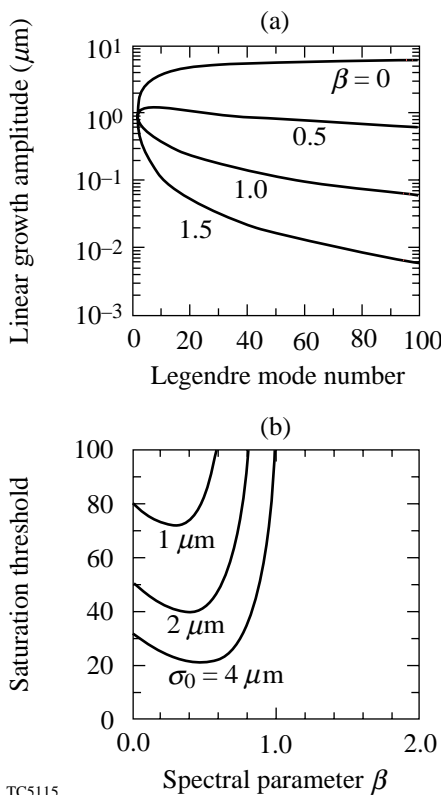
where ℓ_c is defined as the modal saturation threshold. Performing some algebra, assuming $2\ell_c \gg 1$, and defining

$$C_2 = \frac{2}{\sqrt{2\pi C_1}},$$

we have

$$\ell_c = (RC_2)^{1/(1.5-\beta)}.$$

Assuming $R \sim 200 \mu\text{m}$, we can graph the saturation threshold for a variety of initial perturbation rms and spectral parameter β . Such results are plotted over the spectral behavior in Fig. 79.A1. From this graph it can be seen that for β below 1.0, saturation can be expected to play a role in determining the perturbation spectrum at stagnation. For values of β above 1.0, saturation no longer aids in limiting the growth of modes below 100; however, as was pointed out above, in this regime the modal amplitudes fall off quickly with increasing mode number and, as such, will not contribute at stagnation.

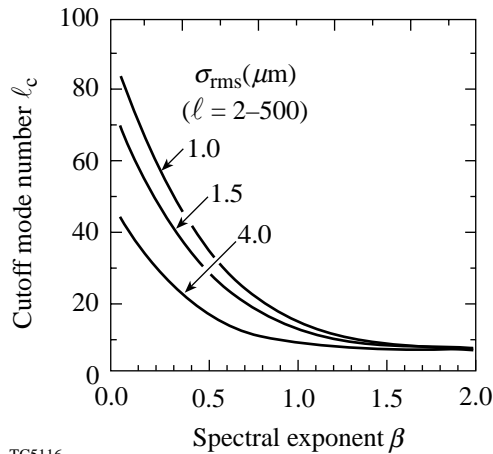


TC5115

Figure 79.A1

(a) Final linear-growth-amplitude spectrum of perturbations with initial amplitudes of the form $\sigma_\ell = C_1/\ell^\beta$. Here C_1 has been normalized to give $1 \mu\text{m}$ at $\ell = 2$ for all cases of β . (b) Saturation threshold (mode number) for various cases of total σ_{rms} as a function of the spectral parameter β . Note that for $\beta > 1$, only modes $\ell > 100$ are candidates for saturation. As the initial spectrum flattens and more power is shifted from lower mode numbers into higher ones, modes above $\ell = 20$ can become candidates for saturation. As β falls below 1.0, saturation can be expected to play an increasing role in determining the final perturbation spectrum at stagnation.

A fully integrated measure of the importance of the modal spectrum can be attained by examining the mode number at stagnation at which the integral of power up to that mode represents 95% of the total perturbed power. A full stability analysis was performed for a variety of spectral parameters β and initial perturbation rms to obtain such a cutoff. The results, shown in Fig. 79.A2, clearly show that, for expected values of β (0.5 to 1.5), 95% of the total power resides in modes less than 50. For values of β below 0.5, the cutoff mode number does climb above 50, but it is well contained below mode 100 for expected rms values.



TC5116

Figure 79.A2

Cutoff mode number at stagnation at which the integral of perturbed power up to that mode represents 95% of the total perturbed power. For expected values of total σ_{rms} (0–4 μm) and β (0.5–1.5), 95% of the total power resides in modes less than 50. For values of β below 0.5 the cutoff mode number does climb above 50, but it is well contained below mode 100 for expected rms values.

REFERENCES

1. R. Betti, V. Lobatchev, and R. L. McCrory, *Phys. Rev. Lett.* **81**, 5560 (1998).
2. J. A. Tarvin *et al.*, in *Interferometry*, edited by G. W. Hopkins (SPIE, Bellingham, WA, 1979), Vol. 192, pp. 239–243.
3. T. P. Bernat, D. H. Darling, and J. J. Sanchez, *J. Vac. Sci. Technol.* **20**, 1362 (1982).
4. K. Kim *et al.*, *J. Vac. Sci. Technol. A* **3**, 1196 (1985).
5. K. Kim and D. L. Krahn, *J. Appl. Phys.* **61**, 2729 (1987).
6. T. R. Pattinson and W. J. Felmlee, *J. Vac. Sci. Technol. A* **6**, 1882 (1988).
7. H. J. Kong, M. D. Wittman, and H. Kim, *Appl. Phys. Lett.* **55**, 2274 (1989).
8. Laboratory for Laser Energetics LLE Review **58**, 83, NTIS document No. DOE/SF/19460-17 (1994). Copies may be obtained from the National Technical Information Service, Springfield, VA 22161.
9. K. Creath, in *Surface Characterization and Testing*, edited by K. Creath (SPIE, Bellingham, WA, 1986), Vol. 680, pp. 19–28.
10. K. Kinnstaetter *et al.*, *Appl. Opt.* **27**, 5082 (1988).
11. K. Creath, in *Progress in Optics XXVI*, edited by E. Wolf (North-Holland, Amsterdam, 1988), pp. 351–393.
12. S. M. Pollaine, S. P. Hatchett, and S. H. Langer, *ICF Annual Report 1994*, 87, Lawrence Livermore National Laboratory, Livermore, CA, UCRL-LR-105820-94 (1994).
13. R. J. Wallace, R. L. McEachern, and W. W. Wilcox, *ICF Annual Report 1994*, 79, Lawrence Livermore National Laboratory, Livermore, CA, UCRL-LR-105820-94 (1994).
14. R. L. McEachern, C. E. Moore, and R. J. Wallace, *J. Vac. Sci. Technol. A* **13**, 983 (1995).
15. R. S. Craxton, LLE, unpublished.
16. Tecplot Data Visualization Software, ©1996 by Amtec Engineering, Inc., P.O. Box 3633, Bellevue, WA 98009-3633.
17. A. V. Oppenheim and R. W. Schaffer, *Discrete-Time Signal Processing* (Prentice-Hall, Englewood Cliffs, NJ, 1989).
18. S. W. Haan, *Phys. Rev. A* **39**, 5812 (1989).
19. J. D. Lindl, *Inertial Confinement Fusion: The Quest for Ignition and Energy Gain Using Indirect Drive* (Springer-Verlag, New York, 1998), pp. 66–67.